Research Square

Preprints are preliminary reports that have not undergone peer review.
They should not be considered conclusive, used to inform clinical practice,
or referenced by the media as validated information.

Age-dependent Aβ misfolding reveals fibril-rich plaque cores surrounded by oligomers during amyloid plaque maturation

Melina Helfrich
Ruhr University Bochum
Thomas Arto
Ruhr University Bochum
Frederik Großerüschkamp
Ruhr University Bochum
Hardy Hagena
Ruhr University Bochum
Denise Manahan-Vaughan
Ruhr University Bochum
Klaus Gerwert
Klaus.gerwert@rub.de

Ruhr University Bochum

Research Article

Keywords: Alzheimer's disease, amyloid-β, 5xFAD, infrared spectroscopic imaging, amyloid plaques, β-sheet, plaque maturation, protein secondary structure, label-free imaging

Posted Date: November 18th, 2026

DOI: https://doi.org/10.21203/rs.3.rs-11626151/v1

License: This work is licensed under a Creative Commons Attribution 4.0 International License.
Read Full License

Additional Declarations: No competing interests reported.

Age-dependent Aβ misfolding reveals fibril-rich plaque cores surrounded by oligomers during amyloid plaque maturation

Melina Helfrich[1], Thomas Arto[1], Frederik Großerüschkamp[1,2], Hardy Hagena[3], Denise Manahan-Vaughan[3], Klaus Gerwert[1]

[1] Ruhr University Bochum, Center for Protein Diagnostics (PRODI), Biospectroscopy, Bochum, Germany
[2] Ruhr University Bochum, Medical Faculty, Department of Translational Biophysics, Bochum, Germany
[3] Ruhr University Bochum, Medical Faculty, Department of Neurophysiology, Bochum, Germany

E-mails and ORCIDs:

Melina Helfrich	melina.helfrich@rub.de	0009-0007-2261-2920
Thomas Arto	thomas.arto@rub.de	0009-0008-4503-9685
Frederik Großerüschkamp	frederik.grosserueschkamp@rub.de	0000-0002-0710-6014
Hardy Hagena	hardy.hagena@rub.de	0000-0002-6421-4732
Denise Manahan-Vaughan	denise.manahan-vaughan@rub.de	0000-0002-9283-9609
Klaus Gerwert (corresponding)	Klaus.gerwert@rub.de	0000-0001-8759-5964

Abstract

Amyloid-β plaque formation is a central feature of Alzheimer's disease. Here, we combined label-free infrared spectroscopic imaging with immunofluorescence microscopy to spatially resolve and monitor structural changes associated with Aβ misfolding in amyloid plaques during aging. These changes were investigated in the 5xFAD mouse model at 2, 4, 6, and 12 months of age (n = 4 per genotype and age group). Transgenic mice exhibited an age-dependent increase in β-sheet content within amyloid plaques, as indicated by spatially resolved infrared spectra, compared with wild-type controls. Within amyloid plaques, the β-sheet-to-α-helix IR intensity ratio increased by approximately 17% between 2 and 6 months and remained comparatively stable at 12 months, despite a continued increase in plaque abundance in brain tissue. At 12 months, spatial analysis revealed a gradual increase in relative β-sheet content from the plaque periphery towards the core, with approximately 24% higher values in the core compared with the surrounding tissue. Furthermore, infrared spectra of amyloid plaques from human Alzheimer's disease brain tissue showed a close resemblance to those obtained from 12-month-old 5xFAD mice. Importantly, the age-dependent spectral changes observed in 5xFAD mice are consistent with spectral characteristics previously reported for amyloid plaques in human Alzheimer's disease brain tissue at different stages of plaque maturation. Together, these findings suggest that, during plaque maturation, Aβ aggregates exhibit a higher degree of fibrillar organization towards the plaque core, reflecting the heterogeneous molecular organization of amyloid plaques. These observations highlight the potential importance of targeting Aβ pathology at early stages of plaque development, before the formation of compact cores enriched in insoluble fibrillar aggregates.

Keywords: Alzheimer's disease; amyloid-β; 5xFAD; infrared spectroscopic imaging; amyloid plaques; β-sheet; plaque maturation; protein secondary structure; label-free imaging

Introduction

Alzheimer's disease (AD) is the most common form of dementia and is neuropathologically characterized by extracellular amyloid-β (Aβ) plaques and intracellular neurofibrillary tau tangles (NFTs) [1, 8, 12]. According to the amyloid cascade hypothesis, sequential cleavage of the amyloid precursor protein (APP) by β- and γ-secretases generates Aβ peptides of varying lengths, primarily Aβ40 and Aβ42, the latter being particularly prone to aggregation. These peptides can self-assemble into oligomers that propagate and enhance tau pathology, form fibrils and ultimately insoluble extracellular amyloid plaques [7, 12, 34].

Amyloid plaques exhibit heterogeneous structural characteristics: Although plaque terminology is not used uniformly across neuropathological studies, a broad distinction can be made between diffuse plaques, characterized by loosely organized and predominantly prefibrillar Aβ deposits, and cored plaques, which contain a compact, highly fibrillar amyloid core [36]. Additional and intermediate plaque morphologies have also been described [19, 36]. A temporal progression from diffuse to increasingly compact and ultimately cored plaque morphologies has been proposed [32, 39, 40]. Plaque morphology is accompanied by differences in the molecular organization and aggregation state of Aβ [32]. Diffuse plaques are predominantly associated with less fibrillar Aβ aggregates, whereas compact plaques exhibit increasing levels of fibrillar β-sheet structures [14, 36]. Classic cored plaques are characterized by a highly fibrillar, β-sheet-rich core surrounded by a corona containing less fibrillar Aβ aggregates [17, 19, 32].

While the morphological progression of amyloid plaques has been extensively described, the structural evolution of Aβ during plaque maturation remains poorly understood [25, 29]. Understanding these structural changes is relevant, as the molecular organization of Aβ may influence aggregation behavior, interactions with cellular components, and the recognition of different Aβ assemblies by therapeutic antibodies [16, 41]. Standard histological methods provide valuable information on plaque localization, morphology, and abundance, but offer only limited insight into the underlying protein secondary structure [19, 36].

An approach that combines immunofluorescence microscopy with infrared (IR) spectroscopic imaging is ideally suited to overcome these limitations. In contrast to conventional histological techniques, IR spectroscopy provides direct biochemical information without the need for structure-specific dyes and is highly sensitive to changes in protein secondary structure [6, 24, 32, 35]. It exploits the interaction of mid-infrared radiation with biological tissue, where molecular vibrations generate characteristic absorption bands that reflect the biochemical composition of the sample [4, 23]. This approach is particularly valuable for investigating proteins such as Aβ, whose secondary structure changes during aggregation [15]. The amide I band contains contributions from α-helical, β-sheet, and random coil structures, enabling the assessment of structural differences within amyloid deposits [5, 24, 38] (Supplementary Fig. S1).

Previous studies using spectroscopic and structure-sensitive imaging approaches have demonstrated considerable conformational heterogeneity of Aβ aggregates and plaques [3, 19, 31, 32]. Nyström et al. [25] further demonstrated age-dependent conformational rearrangements of Aβ deposits, while Fourier-transform infrared (FTIR) spectroscopic studies revealed distinct spectral characteristics of diffuse and dense-core plaques, reflecting differences in β-sheet organization [31, 32]. However, the age-dependent evolution of plaque-associated IR spectral characteristics across defined stages of amyloid pathology within the same experimental model remains incompletely characterized. Investigating these temporal changes requires an animal model that reproducibly develops amyloid pathology over distinct disease stages [20].

We therefore employed the 5xFAD mouse model, which carries five familial AD-linked mutations in APP and PSEN1 [26]. These mutations result in early and robust Aβ deposition, with the first plaques appearing in the subiculum and deep cortical layers at approximately two months of age, followed by progressive accumulation throughout the cortex and hippocampus [9, 26, 27]. This regional and age-dependent progression makes this animal model of AD well suited for studying the temporal evolution of plaque maturation [9, 26, 27].

In the present study, we combined immunofluorescence-guided plaque segmentation with IR spectroscopic imaging to investigate the age-dependent structural evolution of Aβ plaques in the 5xFAD mouse model. By characterizing changes in Aβ secondary structure distribution across multiple disease stages, we aimed to identify molecular signatures associated with plaque maturation and to assess whether plaques exhibit a progressive shift toward β-sheet-rich structures with increasing age. A comparison with human AD tissue was further used to determine whether the structural characteristics of mature plaques in 5xFAD mice resemble those observed in human AD. We hypothesized that Aβ plaques undergo progressive structural changes during disease progression, characterized by an age-dependent increase in β-sheet-associated spectral features.

Methods

The study was conducted in compliance with the European Communities Council Directive of September 22nd 2010 (2010／63／EEC) for care of laboratory animals. Humane endpoints were implemented. Animal well-being was monitored daily and was accompanied by regular health assessments by the veterinary clinician of Ruhr University Bochum

Animals. The study was performed using 5xFAD transgenic (TG) mice that were bred on a C57BL/6 genetic background (B6.Cg-Tg(APPSwFlLon,PSEN1*M146L*L286V) 6799Vas/Mmjax; MMRRC strain #034848-JAX, Jackson Laboratories, Maine, USA) and age-matched wild-type (WT) C57BL/6 controls. Breeding stock was obtained from The Jackson Laboratory (Bar Harbor, Maine, U.S.A.) and offspring mice were bred in-house (Department of Neurophysiology, Medical Faculty, Ruhr University Bochum). Animals were housed in purpose-built vivaria (Scantainer, Scanbur Technology A/S,

Karlslunde, Denmark) with a constant temperature (22 ± 2 °C) and humidity (55 ± 5%). A 12-h light–dark cycle was followed and animals had *ad libitum* access to food and water.

Brains were extracted for examination at 1, 2, 4, 6, and 12 months of age. Each age group comprised four TG and four WT mice, with two females and two males per genotype, resulting in a total of 40 animals. In the 4-month-old TG group, one female dataset was excluded due to a technical stage malfunction that resulted in incorrect acquisition and assembly of the tiled IR image. As no additional female dataset was available for this age group, an available male dataset was used instead, resulting in a final composition of one female and three male mice.

Sample preparation. Immediately following euthanasia by intraperitoneal injection of sodium pentobarbital (200 mg/kg), the abdomen und chest were opened and blood samples (ca. 0.5 ml) were collected by puncturing the left ventricle. Blood was transferred into Eppendorf Safe-Lock® tubes (Eppendorf SE, Hamburg, Germany) that contained 0.5 M ethylenediaminetetraacetic acid (EDTA) dissolved in double distilled water. Afterwards, brains were removed, quick-frozen in isopentane (- 80 °C) and stored at - 80 °C until further processing.

The right hemisphere of each brain was then processed for the analyses described in this study, while the left hemisphere was stored at – 80 °C for follow-up investigations. Coronal cryosections (10 µm) were prepared along the anterior–posterior axis using a cryostat (Leica CM1950, Leica Microsystems, Wetzlar, Germany), with an interval of 200 µm between consecutive sections. Sectioning began at approximately 2.4 mm anterior to Bregma and ended at approximately 3.4 mm posterior to Bregma, as estimated using the mouse brain atlas of Paxinos and Franklin [30]. A total of 30 sections per brain were collected and distributed across three frame slides equipped with 1.4 µm-thick polyethylene terephthalate (PET) membranes (MicroDissect GmbH, Herford, Germany) to enable infrared transmission measurements.

Only sections mounted on the third and final frame slide were included in the analyses. These sections originated from the posterior third of the sectioning series and were selected to represent comparable rostrocaudal levels of the hippocampal formation, including the subiculum, and adjacent cortical regions containing deep cortical layers, across animals, based on consistent anatomical landmarks and comparison with a mouse brain atlas [30]. For the human AD sample (see below), a 10 µm thick section of the middle temporal gyrus was mounted on a PET frame slide for subsequent spectral analysis.

Human brain tissue. Post-mortem middle temporal gyrus tissue from an 82-year-old male donor with AD neuropathological changes (ABC score A3B3C3; Thal amyloid phase 5) was obtained from the Netherlands Brain Bank (NBB; Amsterdam, The Netherlands; project no. 1430). Informed consent for the use of brain tissue and clinical information for research purposes was obtained from the donor or his next of kin, and

NBB procedures were approved by the Institutional Review Board and Medical Ethics Committee of the Vrije Universiteit Medical Center.

Infrared Imaging. Prior to immunofluorescence staining, all tissue sections were analysed by IR imaging to preserve their native biochemical composition. Measurements were performed in transmission mode using a quantum cascade laser-based microscope (LUMOS II ILIM, Bruker Optics GmbH, Ettlingen, Germany) controlled with OPUS software (Bruker Optics GmbH, Ettlingen, Germany). IR images were acquired using a 4x (0.6 NA) objective with a spatial resolution of 4.25 µm and a field of view of approximately 2.2 × 2.0 mm^2 per tile. Full spectra were recorded in sweep scan mode over a spectral range of 1800–952 cm^{-1} with a spectral sampling interval of 2 cm^{-1} and without co-added scans (i.e., one scan per sampling area). To cover the complete tissue section, multiple adjacent image tiles were acquired and subsequently stitched into a single mosaic using an in-house-developed Python script.

A background spectrum of the PET membrane was acquired prior to each tile measurement and automatically subtracted from the corresponding tissue spectra. To assess potential residual contributions from the PET membrane after background correction, spectra from tissue-free PET regions within the acquired IR images were compared with spectra from tissue regions. Residual absorbance in the spectral range relevant to the present analysis (1500–1700 cm^{-1}) was negligible compared with tissue absorbance (Supplementary Fig. S2). Each image pixel contained a full infrared spectrum covering the spectral range from 1802 to 952 cm^{-1}. Spectra were acquired at 2 cm^{-1} intervals, resulting in 426 spectral variables per image pixel. To minimize spectral interference from atmospheric water vapor, tissue sections were thawed under a continuous stream of dry air and maintained under these conditions until immediately before IR imaging.

Immunofluorescence. Brain cryosections were fixed in 4% paraformaldehyde (PFA) for 30 min and subsequently washed three times with phosphate-buffered saline (PBS) for 1 min each. Non-specific binding sites were blocked by incubation in 5% (v/v) mouse serum diluted in Dako REAL Antibody Diluent (Agilent Technologies, Santa Clara, CA, USA) for 45 min. After three washing steps in PBS (3 min each), sections were incubated overnight at 4 °C in a humidified chamber with the following primary antibodies: anti-Aβ (clone: 4G8, directly labelled with Sparky YG 570, 1:1,000; BioLegend, Cat. No. 800722, Lot B413932, RRID: AB_2861076) and anti-CD68 (clone: FA-11, 1:400; Invitrogen, Cat. No. 14-0681-82, Lot 3009288, RRID: AB_2572857).

Following three washes with PBS (3 min each), sections were incubated with 4′,6-diamidino-2-phenylindole (DAPI) (1:10,000; Biotium, Cat. No. 40043, Lot 23D0314) for 15 min, washed thrice with PBS (1 min each), and subsequently incubated for 1 h at room temperature with Alexa Fluor™ 488-conjugated goat anti-rat IgG secondary antibody (1:500; Invitrogen, Thermo Fisher Scientific, Cat. No. A4826, Lot AB411113, RRID: AB_2896334). Finally, sections were washed again thrice with PBS (1 min

each), rinsed with distilled water for 1 min, mounted using EverBrite™ Mounting Medium (Biotium), and allowed to dry.

Fluorescence images were acquired using a slide scanner (Olympus VS120, Olympus Corporation, Tokyo, Japan) equipped with a 20x (0.75 NA) objective with a pixel size of 0.323 µm per pixel. To ensure comparability of fluorescence intensities across tissue sections, exposure times were kept constant for all samples and were set to 100 ms for 4G8 (Sparky YG 570), 100 ms for CD68 (Alexa Fluor 488), and 5 ms for DAPI.

Image Alignment. To enable pixel-wise integration of the immunofluorescence and infrared imaging data, the corresponding datasets were spatially registered. Fluorescence images were first down-sampled threefold in QuPath and subsequently aligned to the corresponding IR images using the BigWarp plugin in Fiji (ImageJ 1.54p). The IR image served as the fixed reference, while the fluorescence image was treated as the moving image. Corresponding anatomical landmarks were manually selected in both modalities and used to calculate a thin-plate spline transformation, which mapped the fluorescence image into the coordinate system of the IR image. An overview of the complete experimental workflow is shown in Fig. 1.

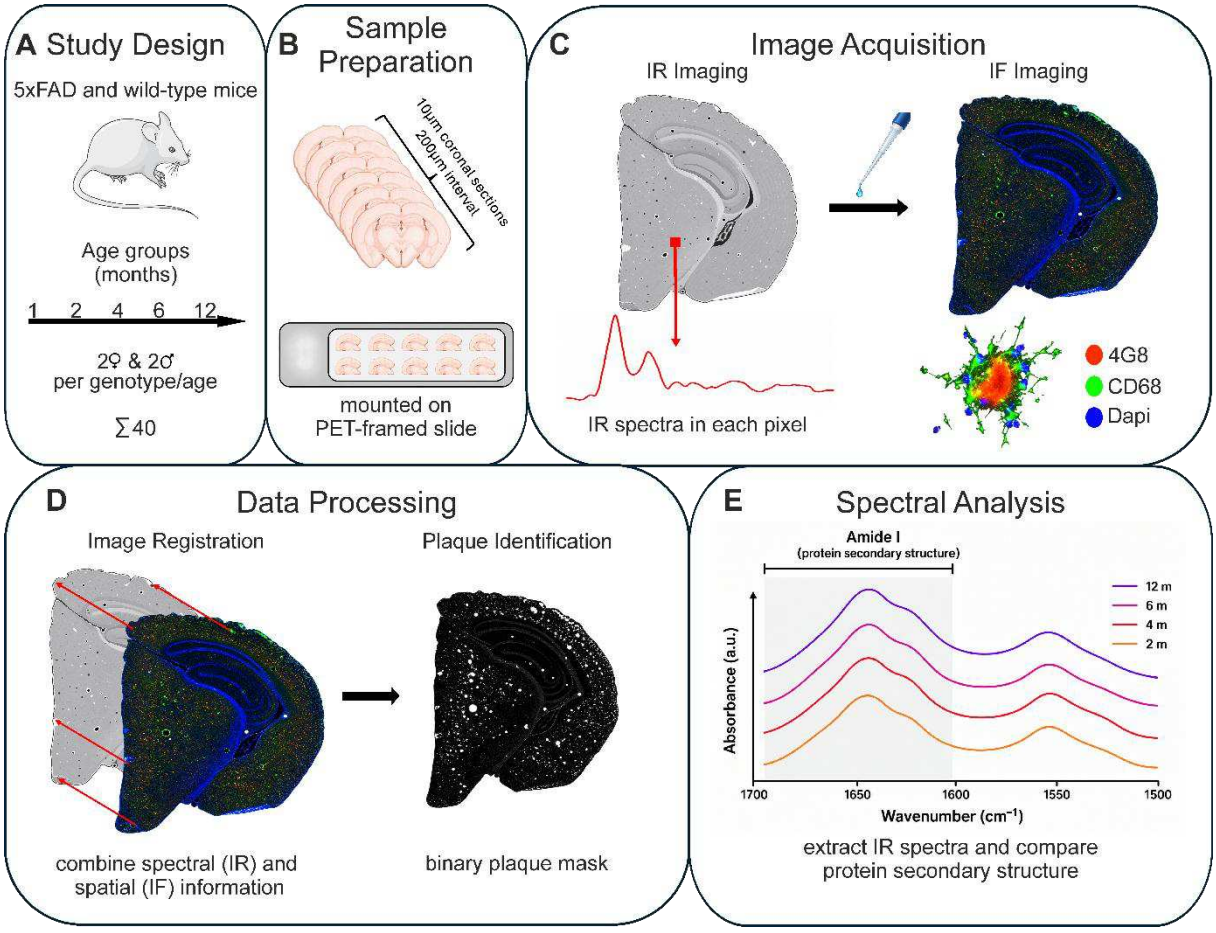


Figure 1. Schematic overview of the experimental workflow. (A) The study included 5xFAD mice and age-matched wild-type controls at 1, 2, 4, 6, and 12 months of age, comprising a total of 40 animals. (B) One hemisphere per brain was sectioned coronally at a thickness of 10 µm and 200 µm intervals. Sections were mounted on PET frame slides suitable for subsequent infrared (IR) transmission measurements. (C) IR images were first acquired from the unstained tissue sections, providing a full IR spectrum at each image pixel. The same sections were subsequently subjected to immunofluorescence staining and imaging to visualize amyloid-β (4G8), microglia

(CD68), and cell nuclei (DAPI). (D) IR and immunofluorescence images were spatially registered, enabling the generation of binary plaque masks based on the 4G8 signal. (E) Plaque-associated IR spectra were extracted using these masks and subjected to further spectral analysis to investigate protein secondary structure.

Data preparation. Prior to spectral analysis, the aligned fluorescence images and corresponding infrared images were visually inspected for artifacts. Regions affected by air bubbles, freezing or staining artifacts, tissue folds, or other image imperfections were manually excluded by generating a binary exclusion mask. Exclusion was restricted to technical artifacts and was independent of plaque presence or spectral characteristics. This mask was applied throughout all subsequent processing steps to ensure that only artifact-free tissue regions were included in the spectral analysis.

Spectral analysis. A custom Python script was developed to automatically extract IR spectra from the registered datasets. For TG animals, Aβ plaques were identified based on the spatially aligned 4G8 immunofluorescence signal. 4G8-positive pixels were segmented using a fixed fluorescence intensity threshold of 75 on an 8-bit scale (0-255), which was applied consistently across all images. Following application of the tissue and exclusion masks, the resulting 4G8-positive pixel coordinates were mapped onto the corresponding IR image, and the associated spectra were extracted and averaged to obtain one representative plaque spectrum per tissue section. For wild-type animals, all pixels classified as tissue, based on the IR absorbance at 1656 cm^{-1} and remaining after application of the exclusion mask, were extracted and averaged to obtain one representative tissue spectrum per section. For each animal, spectra obtained from three analysed tissue sections were averaged to generate one representative spectrum per mouse. Thus, each experimental group (n = 4 animals) comprised a total of 12 analysed tissue sections. For each spectral analysis, a linear baseline was defined between the first and last data points of the respective spectral range and subtracted from the spectrum. Subsequently, each spectrum was vector-normalized over the amide I region (1600–1700 cm^{-1}) by scaling it to unit Euclidean norm. Absorbance around 1630 cm^{-1} is associated with β-sheet-rich protein structures, whereas the contribution around 1656 cm^{-1} predominantly reflects α-helical and disordered protein structures. Accordingly, the I_{1630}/I_{1656} absorbance ratio was used as an indicator of the relative β-sheet-associated spectral contribution and was calculated from the spectral intensities at 1630 and 1656 cm^{-1}. Second-derivative spectra were calculated numerically by two successive gradient operations with respect to wavenumber. No additional Mie-scattering correction was applied, as inspection of the raw spectra did not reveal pronounced scattering-related spectral distortions in the spectral region evaluated (Supplementary Fig. S3). For group-level analyses, the resulting representative spectra were averaged across animals of the same genotype and age.

Unless otherwise stated, all image processing, spectral analyses, and figure generation were performed using custom-developed in-house scripts written in Python (Python Software Foundation, Wilmington, DE, USA).

Spatial plaque analysis. To investigate the spatial distribution of spectral characteristics within and around individual amyloid plaques, the 4G8 fluorescence

intensity was used to subdivide plaque-associated regions into four compartments. The 8-bit intensity values of the red 4G8 fluorescence channel, acquired using identical exposure settings across samples, were linearly scaled from 0–255 to 0–1 by division by 255. Based on the fluorescence intensity scale of the acquired images, pixels with intensities <0.1 were classified as surrounding tissue, intensities from 0.1 to <0.5 as outer corona, intensities from 0.5 to <0.9 as inner corona, and intensities ≥0.9 as plaque core. Following image registration, the fluorescence-defined compartments were mapped onto the corresponding IR images for subsequent spectral analysis. The spatial compartment analysis was restricted to 12-month-old 5xFAD mice, representing the latest investigated stage with abundant and well-developed amyloid plaques. For each 12-month-old 5xFAD mouse, approximately ten plaques were manually selected from each of three tissue sections without selection based on the corresponding IR spectral characteristics. Compartment-specific I_{1630}/I_{1656} ratios were first averaged across plaques within each section and subsequently across the three sections, resulting in one mean value per compartment and animal (n = 4 mice).

Results

IR imaging reveals plaque-associated spectral changes corresponding to 4G8-positive Aβ deposits

Immunofluorescence staining was used to visualize Aβ deposits and their surrounding cellular environment in brain sections of 5xFAD mice. A representative region containing 4G8-positive Aβ plaques, together with CD68-positive microglia and DAPI-stained nuclei, is shown in Fig. 2A.

To investigate whether amyloid plaques can be distinguished based on their infrared spectral properties, IR imaging was performed on the same tissue regions prior to immunofluorescence staining. The I_{1630}/I_{1656} absorbance ratio was spatially mapped across the measured tissue region (Fig. 2B). Regions with elevated I_{1630}/I_{1656} ratios were observed at the locations of 4G8-positive Aβ deposits identified in the corresponding immunofluorescence image. Thus, Aβ-positive plaque regions were associated with an increased β-sheet-associated infrared spectral signature compared with the surrounding tissue.

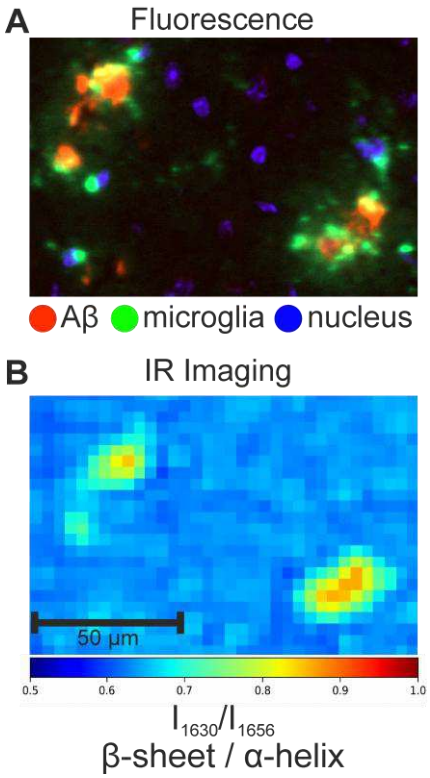


Fig. 2. Correlative immunofluorescence and infrared imaging of amyloid-β plaques. (A) Representative immunofluorescence image showing Aβ deposits (4G8, red), CD68-positive microglia (green), and cell nuclei (DAPI, blue). (B) Corresponding infrared image of the same tissue region visualizing the I_{1630}/I_{1656} absorbance ratio as an indicator of the relative β-sheet-associated spectral contribution. The color scale ranges from 0.5 to 1.0, with warmer colors indicating higher ratios.

Plaque-associated IR spectra reveal age-dependent changes in β-sheet-associated features

To assess whether the spectral characteristics of amyloid plaques in the 5xFAD mouse model resemble those observed in human AD pathology, plaque-associated spectra were additionally extracted from the middle temporal gyrus of one human AD case. The tissue section was analysed using the same workflow of IR imaging, immunofluorescence staining, image registration, and plaque-specific spectral extraction as applied to the mouse tissue. Comparison of the mean plaque-associated spectra revealed similar spectral profiles between human and 12-month-old 5xFAD mouse plaques, particularly with respect to the overall shape of the amide I and amide II bands (Fig. 3A). Thus, plaque-associated IR spectra obtained from the 5xFAD model exhibited spectral characteristics comparable to those observed in human AD tissue.

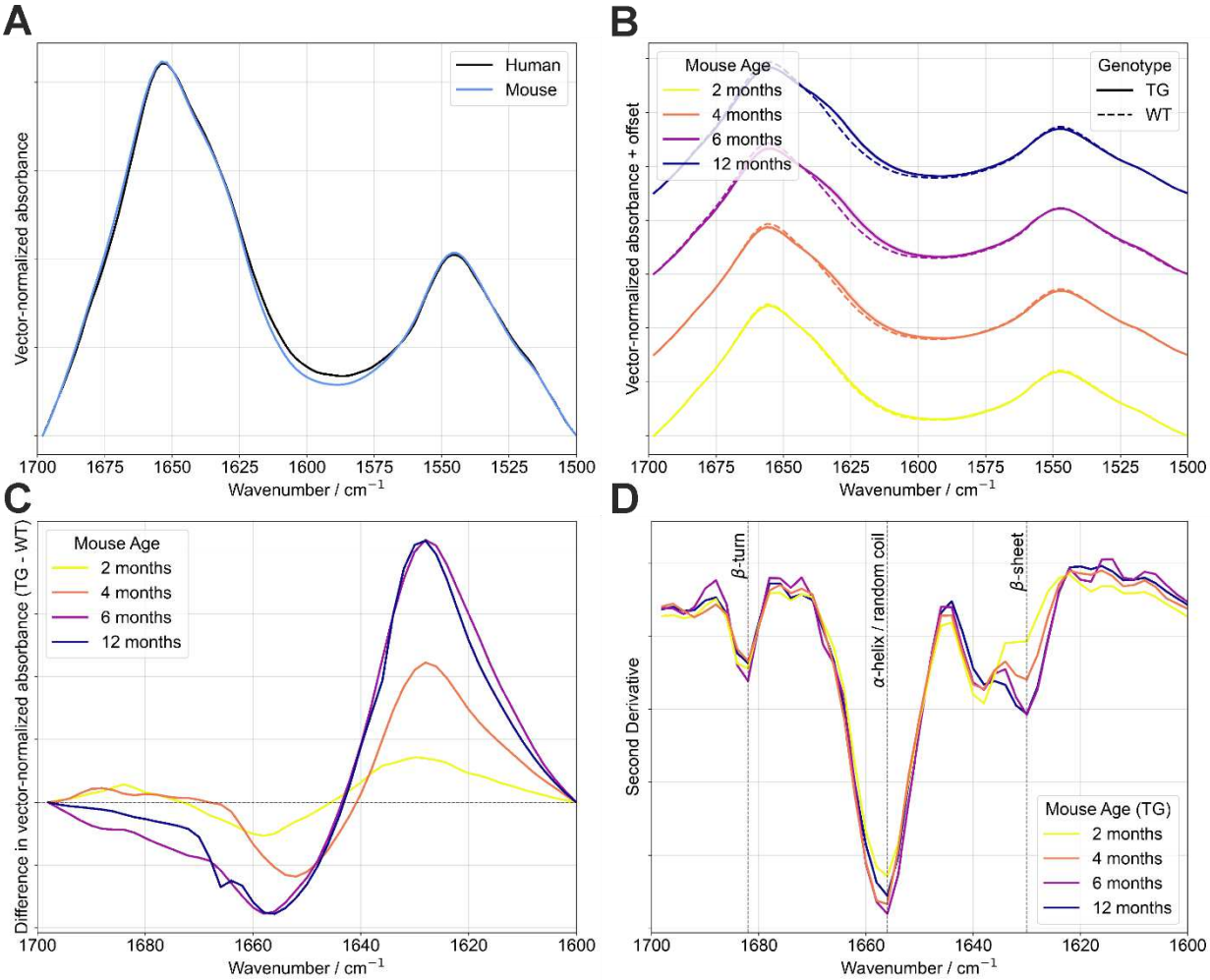


Figure 3: Age-dependent changes in plaque-associated infrared spectra of 5xFAD mice.
A) Comparison of mean plaque-associated IR spectra extracted from the middle temporal gyrus of one human AD case and brain tissue of 12-month-old 5xFAD mice. Spectra were vector-normalized prior to comparison and are shown for the amide I and amide II regions. (B) Mean vector-normalized IR spectra of plaque-associated pixels from 5xFAD mice (TG, solid lines) and tissue pixels from age-matched WT controls (dashed lines) at 2, 4, 6, and 12 months of age (n = 4 mice per group). Shaded areas represent the standard deviation between individual TG mice. For clarity, the standard deviation of WT spectra is not displayed in this panel but is provided in Supplementary Fig. S4, together with the TG variability. (C) Difference spectra calculated from the corresponding vector-normalized mean TG and WT spectra (TG − WT) for each age group. Difference spectra are shown for the amide I region (1600–1700 cm⁻¹). (D) Second-derivative spectra of plaque-associated TG spectra at 2, 4, 6, and 12 months of age within the amide I region. Dashed vertical lines indicate spectral positions associated with β-turn (~1682 cm⁻¹), α-helical/disordered structures (~1656 cm⁻¹), and β-sheet-rich structures (~1630 cm⁻¹). Spectra were vector-normalized prior to comparison. TG, transgenic 5xFAD; WT, wild type; AD, Alzheimer's disease.

To assess whether the plaque-associated spectral signature changes during disease progression, we compared 5xFAD mice with age-matched WT controls. As no 4G8-positive plaques were detected in 1-month-old 5xFAD mice, subsequent plaque-specific analyses were restricted to 2, 4, 6, and 12 months of age (Fig. 3B). TG spectra were derived from plaque-associated regions, whereas WT spectra were derived from tissue regions.

At 2 months of age, the mean TG and WT spectra showed only minor differences. With increasing age, however, the spectral profiles progressively diverged, particularly within the amide I region. The plaque-associated TG spectra showed a decreasing relative contribution around 1656 cm⁻¹ compared with the corresponding WT spectra,

accompanied by an increasingly pronounced contribution in the β-sheet-associated region around 1630 cm^{-1}. The largest spectral changes were observed between 2 and 6 months of age, whereas the profiles at 6 and 12 months were comparatively similar. In contrast to the progressive spectral changes observed in plaque-associated TG spectra, the corresponding WT spectra showed no pronounced age-dependent changes across the investigated age groups.

To further visualize plaque-associated spectral alterations relative to non-plaque tissue, difference spectra were calculated between the mean spectra of 5xFAD plaque pixels and the corresponding age-matched WT tissue spectra (TG-WT; Fig. 3C). As the major spectral differences were observed within the amide I region, subsequent analyses focused on the spectral range between 1600 and 1700 cm^{-1}. With increasing age, an increasingly negative difference developed around 1656 cm^{-1}, accompanied by an increasing positive contribution around 1630 cm^{-1}. This pattern is consistent with a relative redistribution of the amide I spectral contribution from the region around 1656 cm^{-1} toward the β-sheet-associated region around 1630 cm^{-1}. The magnitude of these differences increased predominantly between 2 and 6 months, while only minor additional changes were apparent between 6 and 12 months.

To resolve overlapping contributions within the amide I band in greater detail, second-derivative spectra were calculated (Fig. 3D). Second-derivative analysis enhances partially overlapping spectral components and thereby facilitates the identification of band contributions that are less apparent in the original absorbance spectra. The spectra revealed distinct features in regions associated with different protein secondary structures, including contributions around 1682 cm^{-1}, 1656 cm^{-1}, and 1630 cm^{-1}. Most notably, the β-sheet-associated feature around 1630 cm^{-1} became progressively more pronounced with increasing age, particularly between 2 and 6 months, while only minor additional changes were apparent at 12 months. This age-dependent spectral pattern was subsequently quantified using the I_{1630}/I_{1656} ratio (Fig. 4).

Spatial mapping and quantification reveal age-dependent changes in plaque-associated β-sheet signatures

To investigate the spatial distribution and age-dependent development of the β-sheet-associated spectral changes identified in the plaque spectra, I_{1630}/I_{1656} ratio maps were generated for 5xFAD mice at 2, 4, 6, and 12 months of age. Representative tissue regions from each age group are shown in Fig. 4A using an identical colour scale to allow direct comparison between time points.

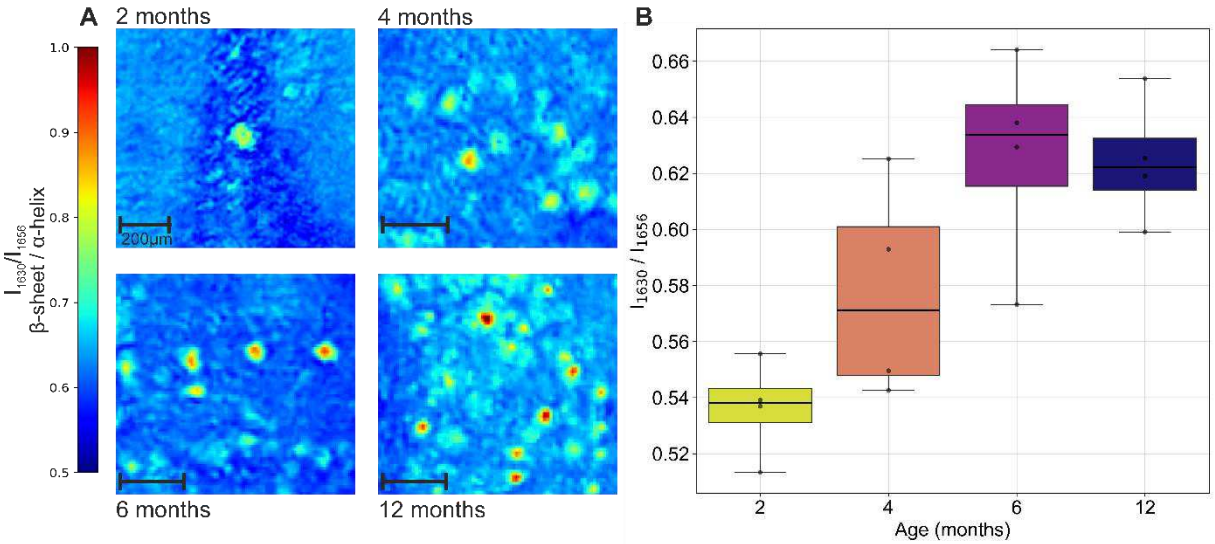


Figure 4. Age-dependent changes in the β-sheet-associated spectral signature of amyloid plaques in 5xFAD mice.

(A) Representative IR ratio maps of brain tissue from 5xFAD mice at 2, 4, 6, and 12 months of age. The I_{1630}/I_{1656} ratio was calculated pixel-wise and visualized using an identical colour scale ranging from 0.5 to 1.0 for all age groups and corresponding to that used in Fig. 2B. Higher ratios indicate an increased relative contribution of the β-sheet-associated spectral region around 1630 cm^{-1}. Scale bars, 200 µm. (B) Quantification of the mean plaque-associated I_{1630}/I_{1656} ratio at 2, 4, 6, and 12 months of age (n = 4 mice per age group). For each mouse, the ratio was averaged across all plaque-associated spectra, resulting in one value per animal. Boxes represent the interquartile range (25th–75th percentile), centre lines indicate the median, and whiskers extend to the most extreme values within 1.5 × the interquartile range. Individual points represent individual mice.

Representative IR ratio maps revealed spatially localized regions of increased I_{1630}/I_{1656} ratios within amyloid plaques compared with the surrounding tissue (Fig. 4A). At 2 months, only small regions with elevated ratios were apparent, whereas higher-ratio regions became increasingly prominent at 4 and 6 months. The spatial ratio patterns at 6 and 12 months appeared broadly comparable, consistent with the spectral observations described above.

To quantify age-dependent changes in the plaque-associated spectral signature across the entire cohort, the mean I_{1630}/I_{1656} ratio was calculated from all plaque-associated spectra of each individual mouse, resulting in one mean ratio per animal (Fig. 4B; n = 4 mice per age group). The median plaque associated I_{1630}/I_{1656} ratio increased from 0.54 at 2 months to 0.57 at 4 months and 0.63 at 6 months, while the median at 12 months remained at a comparable level (0.62). However, the observed differences between age groups did not reach statistical significance (two-sided pairwise Mann-Whitney U tests with Holm correction for multiple comparisons). Thus, the quantitative analysis indicated an age-dependent trend toward increased plaque-associated I_{1630}/I_{1656} ratios up to 6 months, with little further change at 12 months.

Spatial analysis reveals a gradient in β-sheet-associated spectral signatures within Aβ plaques

To further characterize the molecular composition and spatial organization of individual Aβ plaques, plaques from 12-month-old 5xFAD mice were analysed in greater detail. Rather than comparing plaque-associated spectral signatures across age groups, this

analysis focused on spatial variations within individual plaques. A representative tissue region is shown in Fig. 5A-C. The 4G8 fluorescence image revealed several Aβ-positive plaques within the selected tissue region (Fig. 5A). The corresponding IR ratio map showed increased I_{1630}/I_{1656} ratios at the locations of these plaques (Fig. 5B), demonstrating the spatial correspondence between the fluorescence-defined Aβ deposits and the β-sheet-associated IR signal.

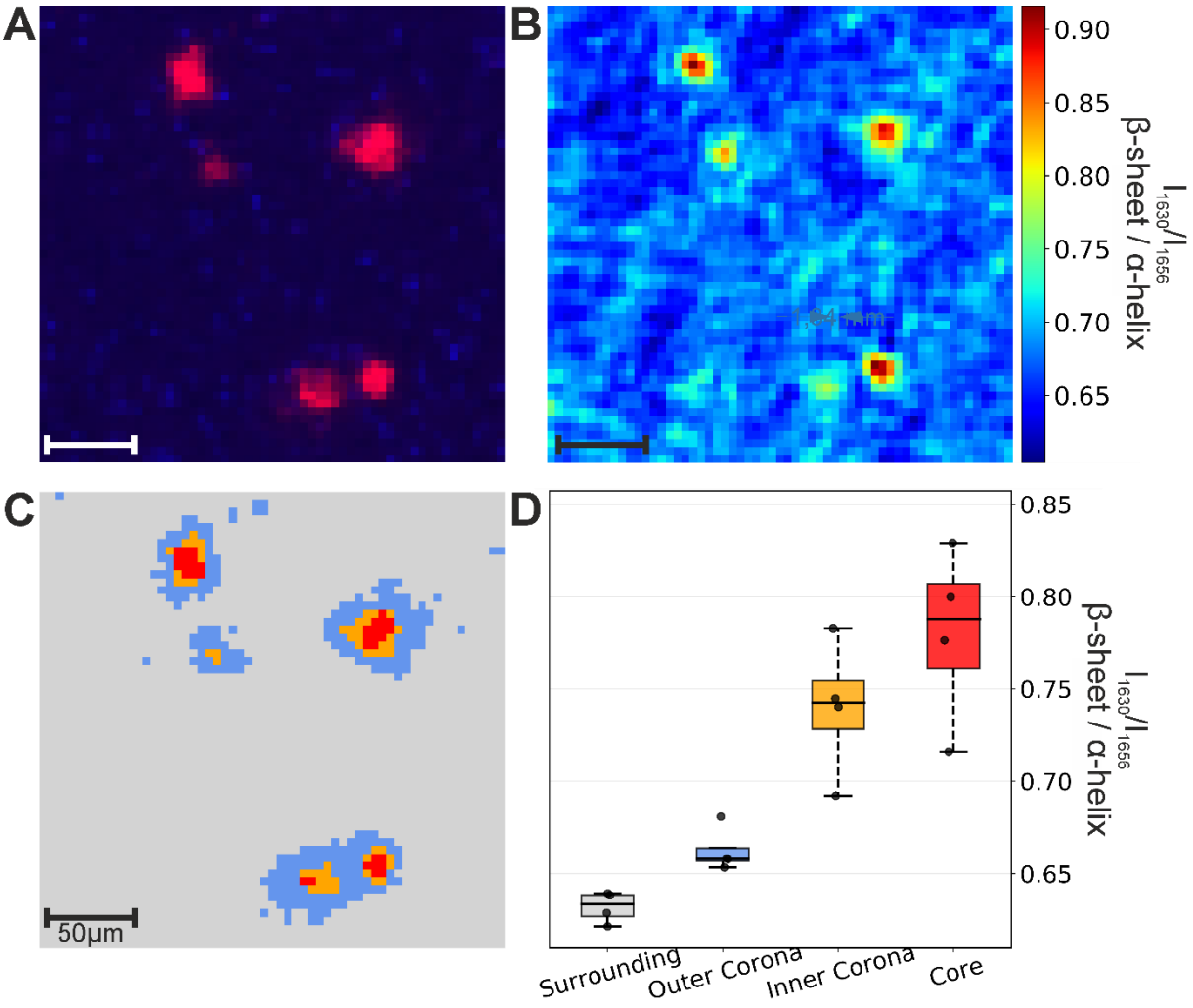


Figure 5. Spatial distribution of the β-sheet-associated spectral signature within amyloid plaques. (A) Representative registered 4G8 immunofluorescence image showing Aβ-positive plaques in a brain tissue section from a 12-month-old 5xFAD mouse. (B) Corresponding IR ratio map of the same tissue region showing the spatial distribution of the I_{1630}/I_{1656} ratio. Higher ratios indicate an increased relative contribution of the β-sheet-associated spectral region around 1630 cm^{-1}. (C) Classification of the same tissue region into surrounding tissue, outer corona, inner corona, and core based scaled 4G8 fluorescence intensity. The original 8-bit fluorescence intensities were linearly scaled from 0–255 to 0–1, and compartments were defined using fluorescence intensity thresholds of 0.1, 0.5, and 0.9, as described in the Methods. (D) Quantification of the mean I_{1630}/I_{1656} ratio within the four fluorescence-defined compartments across 12-month-old 5xFAD mice (n = 4 mice). For each mouse, approximately ten plaques were analysed in each of three tissue sections. Ratios were averaged across plaques within each section and subsequently across the three sections, resulting in one mean value per compartment and animal. Individual points represent individual mice. Boxes represent the interquartile range (25th–75th percentile), centre lines indicate the median, and whiskers extend to the most extreme values within 1.5 × the interquartile range. Scale bars, 50 µm.

For spatial analysis, individual plaques were divided into four fluorescence-defined compartments representing surrounding tissue, outer corona, inner corona, and core (Fig. 5C; see Methods). The compartment-specific I_{1630}/I_{1656} ratios showed a progressive increase from the surrounding tissue toward the plaque core (Fig. 5D; n = 4 mice). Median ratios increased from 0.63 in the surrounding tissue to 0.66 in the outer corona, 0.74 in the inner corona, and 0.79 in the core. Thus, increasing 4G8 fluorescence intensity was spatially associated with higher I_{1630}/I_{1656} ratios toward the plaque core. Given the lower spatial resolution of the IR images compared with the fluorescence images, spectral mixing between plaque-associated and surrounding tissue within individual IR pixels may contribute to the observed gradient.

Discussion

In the present study, IR spectroscopic imaging was used to investigate age-dependent and spatial changes in the molecular organization of amyloid plaques in the 5xFAD mouse model. Three major findings emerged from our analyses. First, 4G8-positive Aβ deposits were characterized by a distinct IR signature with an increased contribution in the β-sheet-associated spectral region around 1630 cm^{-1}. Second, this plaque-associated spectral signature changed with increasing age, with the most pronounced alterations occurring between 2 and 6 months and comparatively minor additional changes between 6 and 12 months. Third, the β-sheet-associated signature was spatially heterogeneous within individual plaques, with increasing I_{1630}/I_{1656} ratios from the surrounding tissue through the fluorescence-defined corona regions toward the plaque core. Together, these findings indicate that the progression of amyloid pathology in 5xFAD mice is accompanied not only by increasing plaque abundance but also by temporal and spatial differences in the molecular organization of plaque-associated material.

The age-dependent spectral changes were particularly evident within the amide I region. With increasing age, the relative contribution around 1630 cm^{-1} increased, while the contribution around 1656 cm^{-1} decreased. The region around 1630 cm^{-1} is commonly associated with β-sheet-rich protein structures, whereas spectral contributions around 1655-1656 cm^{-1} are commonly associated with α-helical structures [10, 18]. Accordingly, the observed changes are consistent with a redistribution of the amide I spectral profile toward an increased contribution of β-sheet-associated structures. This interpretation was further supported by the TG-WT difference spectra and second-derivative analysis, which independently highlighted the increasing prominence of the β-sheet-associated spectral component with age. Since the formation of ordered β-sheet-rich structures is a characteristic feature of amyloid fibrillization [35], the observed spectral changes are compatible with increasing molecular organization and fibrillization of plaque-associated Aβ during plaque development. Because IR spectroscopy measures the overall biochemical composition within a probed volume, the recorded amide I band inherently reflects a superposition of all sampled proteins [22]. In AD brain tissue specifically, this leads to spectral overlap and dilution of plaque-associated Aβ signals by surrounding matrix proteins in the

microenvironment [11]. The spectral changes should therefore be interpreted as changes in the molecular organization of plaque-associated material rather than as a direct quantitative measurement of the β-sheet content of Aβ.

This age-dependent development is particularly interesting in the context of the morphological heterogeneity of amyloid plaques described in human AD tissue. Different plaque morphologies, ranging from diffuse deposits to compact and classic cored plaques, have been suggested to represent different stages of plaque development [13, 39, 40]. In line with this concept, Röhr et al. [32] used vibrational spectroscopic imaging of human AD tissue and reported increasing Aβ fibrillation along the proposed sequence from diffuse to compact and classic cored plaques. The age-dependent increase in the β-sheet-associated spectral signature observed in the present study provides complementary evidence from the 5xFAD model. If these plaque morphologies indeed represent sequential stages of plaque development, our findings are consistent with a progressive molecular reorganization of plaque-associated Aβ toward a more β-sheet-rich and fibrillar state during disease progression [14, 36, 39, 40]. However, as the present study is cross-sectional, it cannot demonstrate the structural transformation of individual plaques over time.

Notably, the most pronounced changes in the plaque-associated spectral signature occurred between 2 and 6 months of age, whereas comparatively little additional change was observed between 6 and 12 months. This period broadly overlaps with the emergence of cognitive and behavioural impairments reported in the 5xFAD model, including deficits in learning and memory from approximately 4–6 months of age [27]. Although this temporal correspondence is noteworthy, a direct relationship between plaque-associated molecular reorganization and functional impairment cannot be inferred from the present study, as behavioural testing was not performed.

In contrast to the comparatively small spectral changes between 6 and 12 months, the abundance of Aβ plaques continued to increase at later ages, consistent with the well-established progression of amyloid pathology in the 5xFAD model [2, 9, 26]. This apparent dissociation suggests that plaque accumulation and changes in plaque-associated molecular organization may not necessarily progress in parallel. One possible explanation is that major changes in the molecular organization of plaque-associated proteins occur relatively early during plaque development, whereas later disease stages are characterized predominantly by continued plaque accumulation and growth with comparatively smaller changes in the average secondary-structure-associated spectral signature. Previous studies in 5xFAD mice have demonstrated pronounced age-dependent increases in plaque burden and changes in plaque morphology and composition, supporting the concept that different aspects of plaque pathology may follow distinct temporal trajectories [2, 9]. Consequently, the increase in amyloid pathology at later ages may primarily reflect an increase in the amount of deposited material rather than an equally pronounced continuation of structural reorganization.

The spatially resolved analyses further support the concept that amyloid plaques are molecularly heterogeneous structures. At 12 months of age, the I_{1630}/I_{1656} ratio progressively increased from the surrounding tissue through the fluorescence-defined outer and inner corona toward the plaque core, with the highest ratios observed in the core regions exhibiting the strongest 4G8 fluorescence. Thus, the β-sheet-associated spectral signature showed a clear spatial gradient toward the plaque core. Beyond its structural implications, plaque compaction is also relevant to the surrounding neuropathology, as microglia have been shown to contribute to the formation of compact amyloid deposits and to limit the exposure of nearby neurites to potentially damaging amyloid structures [43]. This spatial organization is consistent with previous observations in human AD tissue, where classic cored plaques have been shown to contain a highly β-sheet-rich fibrillar core surrounded by regions with lower β-sheet levels [21, 32]. The pronounced β-sheet-associated signature observed within the plaque core therefore supports a higher degree of fibrillar organization in these regions and complements previous histopathological observations of structural differences between plaque core and periphery [21, 32, 39]. Although the I_{1630}/I_{1656} ratio does not directly quantify fibrillar content, its progressive increase from the plaque periphery toward the core is consistent with the established fibrillar organization of cored amyloid plaques [28, 32].

Based on the observed age-dependent and spatial differences in the β-sheet-associated IR signature, we propose a conceptual model of plaque maturation (Fig. 6). In this model, plaques with relatively weak β-sheet-associated signatures are hypothesized to progress toward structures exhibiting increasingly pronounced β-sheet-associated signals, particularly within their cores. Inspired by the conceptual framework proposed by Röhr et al. [32], this progression is illustrated by a hypothetical change in the spatial distribution of Aβ aggregation states, with an increasing contribution of fibrillar structures toward the plaque center. Importantly, the proposed sequence does not represent a directly observed transformation of individual plaques, and the spatial distribution of different Aβ aggregation states cannot be determined unambiguously from the IR measurements alone.

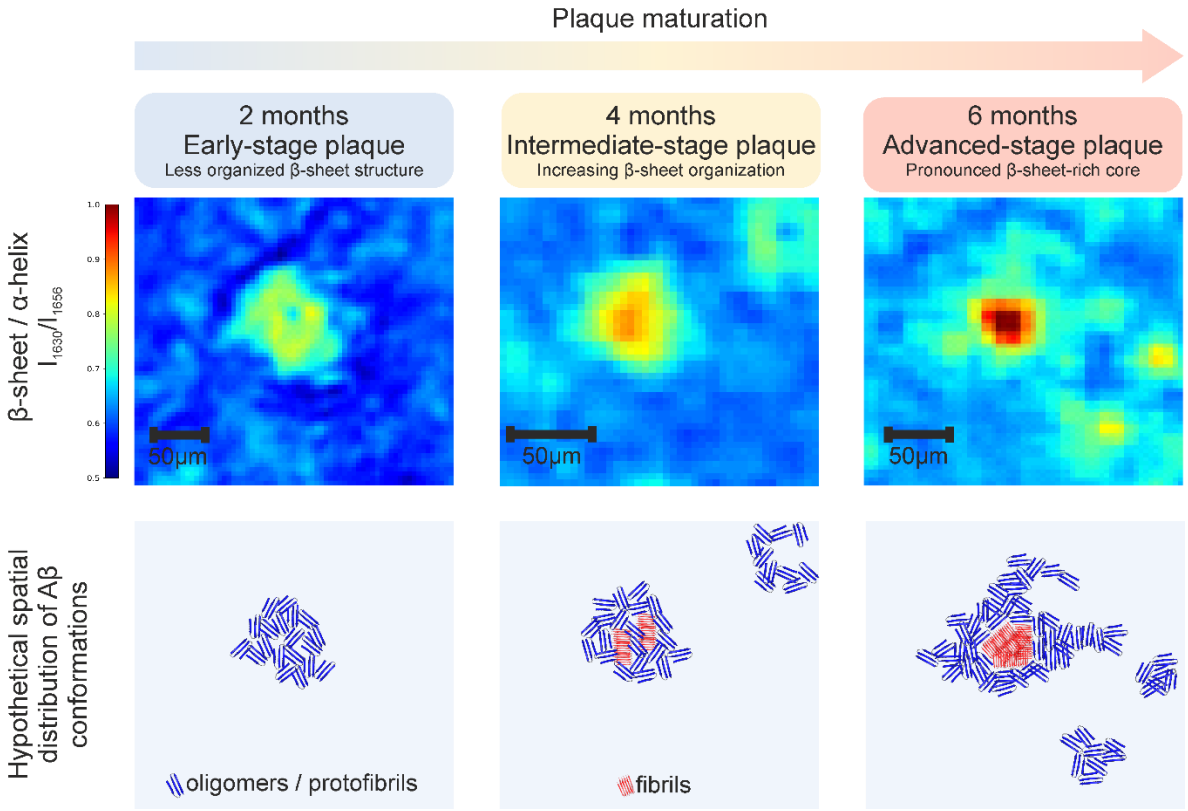


Figure 6. Proposed model of amyloid plaque maturation based on β-sheet-associated IR signatures. Representative IR ratio images (I_{1630}/I_{1656}) of amyloid plaques from 2-, 4-, and 6-month-old 5xFAD mice, illustrating increasingly pronounced β-sheet-associated spectral signatures with age, ranging from relatively weak signals to a prominent core-associated signal. The corresponding schematic illustrations depict a hypothetical spatial distribution of Aβ conformations, with oligomers/protofibrils (blue) and fibrillar structures (red). The proposed maturation sequence integrates the observed age-dependent spectral changes and spatial heterogeneity within amyloid plaques. The illustrations are conceptual and do not represent direct identification of individual Aβ aggregation states or longitudinal observations of plaque maturation. The conceptual representation was inspired by the model proposed by Röhr et al. [32].

The comparison with human AD tissue provides an additional, although preliminary, translational perspective. The plaque-associated spectrum obtained from the human AD tissue exhibited major spectral characteristics similar to those observed in 12-month-old 5xFAD mice, particularly within the amide I region. This qualitative similarity suggests that relevant molecular characteristics of human amyloid pathology are reflected in the 5xFAD model and supports the biological relevance of the spectral changes observed in the mouse tissue. However, only a single human AD case was investigated in the present study. The comparison should therefore be considered illustrative and cannot establish direct molecular equivalence between murine and human amyloid plaques. Differences in plaque morphology between 5xFAD mice and human AD tissue further complicate the interpretation of these spectral similarities. While fibrillar and dense-core plaques are prominent in 5xFAD mice, classical diffuse plaques have been reported to be less prominent or even absent, depending on the brain region and morphological criteria [2, 37]. Furthermore, despite expressing human Aβ, 5xFAD mice reproduce only part of the molecular alterations observed in human AD, and differences in the biochemical composition of the plaque microenvironment may influence the corresponding IR spectral signatures [42]. Future studies including larger and neuropathologically characterized human cohorts will be required to

determine whether the age- and plaque-associated spectral patterns identified in 5xFAD mice correspond to different plaque morphologies or disease stages in human AD.

Moreover, additional limitations should be considered. The relatively small number of animals per age group limits the statistical power to detect subtle differences between age groups and plaque compartments, although each animal-level measurement was derived from a large number of individual plaque-associated spectra across multiple tissue sections. Additionally, the unequal sex distribution in the 4-month-old transgenic group may introduce variability, as sex-dependent differences in amyloid pathology have been reported in the 5xFAD model. The observed temporal and spatial patterns should therefore be interpreted accordingly. Furthermore, although the spatial correspondence between the IR signature and 4G8-positive deposits strongly links the observed spectral changes to amyloid pathology, IR spectroscopy is not molecularly specific for Aβ, and contributions from other plaque-associated proteins or cellular components cannot be excluded. Finally, the cross-sectional experimental design does not allow the structural development of the same plaque to be followed over time. Longitudinal approaches capable of monitoring individual plaques would therefore be particularly valuable for determining whether the spectral differences observed across age groups indeed represent sequential stages of plaque maturation.

In conclusion, our findings indicate that amyloid pathology in 5xFAD mice is accompanied by age-dependent and spatial differences in the β-sheet-associated spectral signature of plaque-associated tissue. The most pronounced changes occurred during earlier stages of plaque development, with comparatively little additional spectral change at later ages. Within individual plaques, the β-sheet-associated signature increased from the surrounding tissue toward fluorescence-defined core regions. Together, these findings are consistent with a proposed model of plaque maturation involving changes in molecular organization, characterized by an increasingly pronounced β-sheet-associated signature toward the plaque core. They further highlight the potential of IR imaging to investigate structural changes in amyloid pathology.

Abbreviations AD: Alzheimer’s Disease; Aβ: amyloid-β; APP: amyloid precursor protein; DAPI: 4′,6-diamidino-2-phenylindole; EDTA: ethylenediaminetetraacetic acid; FTIR: Fourier-transform infrared; IR: Infrared; NFTs: neurofibrillary tau tangles; PBS: phosphate-buffered saline; PET: polyethylene terephthalate; PFA: paraformaldehyde; TG: transgenic; WT: wildtype

Declarations:

Ethics approval and consent to participate

The study was conducted in compliance with the European Communities Council Directive of September 22nd 2010 (2010 / 63 / EEC) for care of laboratory animals. Humane endpoints were implemented. Animal well-being was monitored daily and was accompanied by regular health assessments by the veterinary clinician of Ruhr University Bochum. Donors or their next of kin signed informed consent for the usage of brain tissue and clinical information for research purposes. The Institutional Review Board and Medical Ethical Board (METC) from the Vrije University Medical Center (VUmc) approved the procedures of the NBB.

Consent for publication

Not applicable

Availability of data and material

The data that support the findings of this study are available from the corresponding author K.G. upon reasonable request.

Competing interests

The authors declare no competing financial interests.

Funding

This research was funded by the Alzheimer Forschung Initiative e.V. (AFI, Grant Number: 22022) and by the Center of Protein Diagnostics (PRODI), funded by the Ministry of Innovation (Project Number: 111.08.03.05-133974), Science and Research of North-Rhine Westphalia, Germany.

Author contributions

MH, FG, HH, DMV and KG designed research
MH and TA performed research
MH analysed data
MH wrote the paper
TA, FG, HH, DMV and KG revised the paper
All authors read and approved the final manuscript.

Acknowledgement The authors gratefully acknowledge the research group of Dr. Sebastian Zundler, Department of Medicine 1, University Hospital Erlangen, for providing access to their instrumentation for selected measurements. We further thank Eliena Ibnukhsein and Suzan Polat for their assistance with experimental work, Jens Collitti-Klausnitzer for technical support in brain extractions and Nadine Kollosh for animal care.

References

[1] Alzheimer's Association (2025) 2025 Alzheimer's disease facts and figures. Alzheimers Dement 21. doi:10.1002/alz.70235

[2] Bader AS, Gnädig MU, Fricke M, Büschgens L, Berger LJ, Klafki HW, et al (2023) Brain region-specific differences in amyloid-β plaque composition in 5XFAD mice. Life (Basel) 13:1053. doi:10.3390/life13041053

[3] Baghel D, Naik T, Banerjee S, Edmonds HO, Ghosh A (2026) From disordered to ordered: nanoscale spectroscopy reveals structural evolution of amyloid beta 40 fibrils. ChemPhysChem 27. doi:10.1002/cphc.202500818

[4] Baker MJ, Trevisan J, Bassan P, Bhargava R, Butler HJ, Dorling KM, et al (2014) Using Fourier transform IR spectroscopy to analyze biological materials. Nat Protoc 9:1771–1791. doi:10.1038/nprot.2014.110

[5] Barth A (2007) Infrared spectroscopy of proteins. Biochim Biophys Acta 1767:1073–1101. doi:10.1016/j.bbabio.2007.06.004

[6] Benseny-Cases N, Klementieva O, Cotte M, Ferrer I, Cladera J (2014) Microspectroscopy (μFTIR) reveals co-localization of lipid oxidation and amyloid plaques in human Alzheimer disease brains. Anal Chem 86:12047–12054. doi:10.1021/ac502667b

[7] Bloom GS (2014) Amyloid-β and tau: the trigger and bullet in Alzheimer disease pathogenesis. JAMA Neurol 71:505–508. doi:10.1001/jamaneurol.2013.5847

[8] Braak H, Braak E, Grundke-Iqbal I, Iqbal K (1986) Occurrence of neuropil threads in the senile human brain and in Alzheimer’s disease: a third location of paired helical filaments outside of neurofibrillary tangles and neuritic plaques. Neurosci Lett 65:351–355. doi:10.1016/0304-3940(86)90288-0

[9] Forner S, Kawauchi S, Balderrama-Gutierrez G, Kramár EA, Matheos DP, Phan J, et al (2021) Systematic phenotyping and characterization of the 5xFAD mouse model of Alzheimer’s disease. Sci Data 8:270. doi:10.1038/s41597-021-01054-y

[10] Goormaghtigh E, Ruysschaert JM, Raussens V (2006) Evaluation of the information content in infrared spectra for protein secondary structure determination. Biophys J 90:2946–2957. doi:10.1529/biophysj.105.072017

[11] Gough KM, Tzadu L, Kastyak MZ, Kuzyk AC, Julian RL (2010) Theoretical and experimental considerations for interpretation of amide I bands in tissue. Vib Spectrosc 53:71–76. doi:10.1016/j.vibspec.2010.01.015

[12] Hardy JA, Higgins GA (1992) Alzheimer’s disease: the amyloid cascade hypothesis. Science 256:184–185. doi:10.1126/science.1566067

[13] Ikeda SI, Yanagisawa N, Allsop D, Glenner GG (1990) Early senile plaques in Alzheimer's disease demonstrated by histochemistry, immunocytochemistry, and

electron microscopy. Hum Pathol 21:1221–1226. doi:10.1016/S0046-8177(06)80034-1

[14] Irvine GB, El-Agnaf OM, Shankar GM, Walsh DM (2008) Protein aggregation in the brain: the molecular basis for Alzheimer's and Parkinson's diseases. Mol Med 14:451–464. doi:10.2119/2007-00100.Irvine

[15] Jarrett JT, Lansbury PT (1993) Seeding "one-dimensional crystallization" of amyloid: a pathogenic mechanism in Alzheimer's disease and scrapie? Cell 73:1055–1058. doi:10.1016/0092-8674(93)90635-4

[16] Johannesson M, Söderberg L, Zachrisson O, Fritz N, Kylefjord H, Gkanatsiou E, et al (2024) Lecanemab demonstrates highly selective binding to Aβ protofibrils isolated from Alzheimer's disease brains. Mol Cell Neurosci 130:103949. doi:10.1016/j.mcn.2024.103949

[17] Koffie RM, Meyer-Luehmann M, Hashimoto T, Adams KW, Mielke ML, Garcia-Alloza M, et al (2009) Oligomeric amyloid β associates with postsynaptic densities and correlates with excitatory synapse loss near senile plaques. Proc Natl Acad Sci USA 106:4012–4017. doi:10.1073/pnas.0811698106

[18] Kong J, Yu S (2007) Fourier transform infrared spectroscopic analysis of protein secondary structures. Acta Biochim Biophys Sin (Shanghai) 39:549–559. doi:10.1111/j.1745-7270.2007.00320.x

[19] Koutarapu S, Ge J, Dulewicz M, Srikrishna M, Szadziewska A, Wood J, et al (2025) Chemical imaging delineates Aβ plaque polymorphism across the Alzheimer's disease spectrum. Nat Commun 16:3889. doi:10.1038/s41467-025-59085-7

[20] Lee JE, Han PL (2013) An update of animal models of Alzheimer disease with a reevaluation of plaque depositions. Exp Neurobiol 22:84–95. doi:10.5607/en.2013.22.2.84

[21] Michael R, Lenferink A, Vrensen GFJM, Gelpi E, Barraquer RI, Otto C (2017) Hyperspectral Raman imaging of neuritic plaques and neurofibrillary tangles in brain tissue from Alzheimer's disease patients. Sci Rep 7:15603. doi:10.1038/s41598-017-16002-3

[22] Miller LM, Dumas P (2010) From structure to cellular mechanism with infrared microspectroscopy. Curr Opin Struct Biol 20:649–656. doi:10.1016/j.sbi.2010.07.007

[23] Movasaghi Z, Rehman S, ur Rehman I (2008) Fourier transform infrared (FTIR) spectroscopy of biological tissues. Appl Spectrosc Rev 43:134–179. doi:10.1080/05704920701829043

[24] Nabers A, Ollesch J, Schartner J, Kötting C, Genius J, Haußmann U, et al (2016) An infrared sensor analysing label-free the secondary structure of the Abeta peptide in presence of complex fluids. J Biophotonics 9:224–234. doi:10.1002/jbio.201400145

[25] Nyström S, Psonka-Antonczyk KM, Ellingsen PG, Johansson LBG, Reitan N, Handrick S, et al (2013) Evidence for age-dependent in vivo conformational rearrangement within Aβ amyloid deposits. ACS Chem Biol 8:1128–1133. doi:10.1021/cb4000376

[26] Oakley H, Cole SL, Logan S, Maus E, Shao P, Craft J, et al (2006) Intraneuronal beta-amyloid aggregates, neurodegeneration, and neuron loss in transgenic mice with five familial Alzheimer's disease mutations: potential factors in amyloid plaque formation. J Neurosci 26:10129–10140. doi:10.1523/JNEUROSCI.1202-06.2006

[27] Pádua MS, Guil-Guerrero JL, Lopes PA (2024) Behaviour hallmarks in Alzheimer's disease 5xFAD mouse model. Int J Mol Sci 25:6766. doi:10.3390/ijms25126766

[28] Palombo F, Tamagnini F, Jeynes JCG, Mattana S, Swift I, Nallala J, et al (2018) Detection of Aβ plaque-associated astrogliosis in Alzheimer's disease brain by spectroscopic imaging and immunohistochemistry. Analyst 143:850–857. doi:10.1039/c7an01747b

[29] Parvin F, Haglund S, Wegenast-Braun B, Jucker M, Saito T, Saido TC, et al (2024) Divergent age-dependent conformational rearrangement within Aβ amyloid deposits in APP23, APPPS1, and AppNL-F mice. ACS Chem Neurosci 15:2058–2069. doi:10.1021/acschemneuro.4c00104

[30] Paxinos G, Franklin KBJ (2019) The mouse brain in stereotaxic coordinates, digital version. London: Academic Press

[31] Rak M, Del Bigio MR, Mai S, Westaway D, Gough K (2007) Dense-core and diffuse Aβ plaques in TgCRND8 mice studied with synchrotron FTIR microspectroscopy. Biopolymers 87:207–217. doi:10.1002/bip.20820

[32] Röhr D, Boon BDC, Schuler M, Kremer K, Hoozemans JJM, Bouwman FH, et al (2020) Label-free vibrational imaging of different Aβ plaque types in Alzheimer's disease reveals sequential events in plaque development. Acta Neuropathol Commun 8:222. doi:10.1186/s40478-020-01091-5

[33] Sadat A, Joye IJ (2020) Peak fitting applied to Fourier transform infrared and Raman spectroscopic analysis of proteins. Appl Sci 10:5918. doi:10.3390/app10175918

[34] Sakono M, Zako T (2010) Amyloid oligomers: formation and toxicity of Aβ oligomers. FEBS J 277:1348–1358. doi:10.1111/j.1742-4658.2010.07568.x

[35] Sarroukh R, Cerf E, Derclaye S, Dufrêne YF, Goormaghtigh E, Ruysschaert JM, et al (2011) Transformation of amyloid β(1-40) oligomers into fibrils is characterized by a major change in secondary structure. Cell Mol Life Sci 68:1429–1438. doi:10.1007/s00018-010-0529-x

[36] Serrano-Pozo A, Frosch MP, Masliah E, Hyman BT (2011) Neuropathological alterations in Alzheimer disease. Cold Spring Harb Perspect Med 1. doi:10.1101/cshperspect.a006189

[37] Smith AJ, Duan T, Verkman AS (2019) Aquaporin-4 reduces neuropathology in a mouse model of Alzheimer's disease by remodeling peri-plaque astrocyte structure. Acta Neuropathol Commun 7:74. doi:10.1186/s40478-019-0728-0

[38] Surewicz WK, Mantsch HH, Chapman D (1993) Determination of protein secondary structure by Fourier transform infrared spectroscopy: a critical assessment. Biochemistry 32:389–394. doi:10.1021/bi00053a001

[39] Thal DR, Rüb U, Schultz C, Sassin I, Ghebremedhin E, Del Tredici K, et al (2000) Sequence of Aβ-protein deposition in the human medial temporal lobe. J Neuropathol Exp Neurol 59:733–748. doi:10.1093/jnen/59.8.733

[40] Thal DR, Capetillo-Zarate E, Del Tredici K, Braak H (2006) The development of amyloid beta protein deposits in the aged brain. Sci Aging Knowledge Environ 2006. doi:10.1126/sageke.2006.6.re1

[41] Xu H, Zheng Y, Bai G, Wang Y, Ma B (2026) Differential conformational selections of three therapeutic antibodies binding to polymorphic Aβ oligomers. Int J Biol Macromol 341:150222. doi:10.1016/j.ijbiomac.2026.150222

[42] Yarbro JM, Han X, Dasgupta A, Yang K, Liu D, Shrestha HK, et al (2025) Human and mouse proteomics reveals the shared pathways in Alzheimer’s disease and delayed protein turnover in the amyloidome. Nat Commun 16:1533. doi:10.1038/s41467-025-56853-3

[43] Yuan P, Condello C, Keene CD, Wang Y, Bird TD, Paul SM, et al (2016) TREM2 haplodeficiency in mice and humans impairs the microglia barrier function leading to decreased amyloid compaction and severe axonal dystrophy. Neuron 90:724–739. doi:10.1016/j.neuron.2016.05.003

Supplementary Files

This is a list of supplementary files associated with this preprint. Click to download.

- AgedependentAmisfoldingrevealsfibrilrichplaquecoressurroundedbyoligomersduringamyloidplaquematurationSupplementaryMaterial.docx